

# Simple Analytical and Graphical Methods for Carrier-Based PWM-VSI Drives

Ahmet M. Hava, *Student Member, IEEE*, Russel J. Kerkman, *Fellow, IEEE*, and Thomas A. Lipo, *Fellow, IEEE*

**Abstract**—This paper provides analytical and graphical methods for the study, performance evaluation, and design of the modern carrier-based pulsewidth modulators (PWM's), which are widely employed in PWM voltage-source inverter (VSI) drives. Simple techniques for generating the modulation waves of the high-performance PWM methods are described. The two most important modulator characteristics—the current ripple and the switching losses—are analytically modeled. The graphical illustration of these often complex multivariable functions accelerate the learning process and help one understand the microscopic (per-carrier cycle) and macroscopic (per fundamental cycle) behavior of all the modern PWM methods. The analytical formulas and graphics are valuable educational tools. They also aid the design and implementation of the high-performance PWM methods.

**Index Terms**—Analysis, graphics, harmonics, inverter, modulation, PWM, switching losses, voltage linearity, VSI.

## I. INTRODUCTION

VOLTAGE-SOURCE inverters (VSI's) are utilized in ac motor drive, utility interface, and uninterruptible power supply (UPS) applications as a means for dc  $\leftrightarrow$  ac electric energy conversion. Shown in Fig. 1, the classical VSI generates a low-frequency output voltage with controllable magnitude and frequency by programming high-frequency voltage pulses. Of the various pulse-programming methods, the carrier-based pulsewidth modulation (PWM) methods are the preferred approach in most applications due to the low-harmonic distortion waveform characteristics with well-defined harmonic spectrum, the fixed switching frequency, and implementation simplicity.

Carrier-based PWM methods employ the “per-carrier cycle volt-second balance” principle to program a desirable inverter output-voltage waveform. Two main implementation techniques exist: the triangle intersection technique and the direct digital technique. In the triangle intersection technique, for example, in the sinusoidal PWM (SPWM) method [1], as shown in Fig. 2, the reference modulation wave is compared with a triangular carrier wave and the intersections define the switching instants. As illustrated in the space-vector diagram in Fig. 3, the time length of the inverter states in the direct

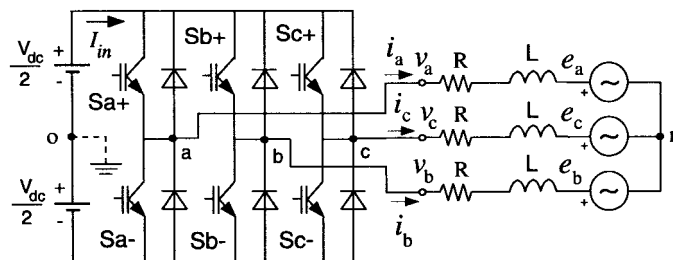


Fig. 1. Circuit diagram of a PWM-VSI drive connected to an R-L-E-type load.

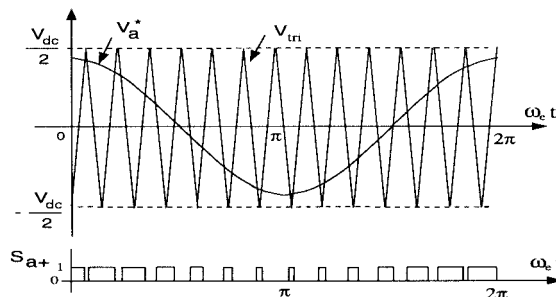


Fig. 2. Triangle intersection PWM phase “a” modulation and switching signals.

digital technique are precalculated for each carrier cycle by employing space-vector theory, and the voltage pulses are directly programmed [2], [3]. With the volt-second balance principle being quite simple, a variety of PWM methods have appeared in the technical literature; each method results from a unique placement of the voltage pulses in isolated neutral-type loads.

In most three-phase ac motor drive and utility interface applications, the neutral point is isolated and no neutral current path exists. In such applications, in the triangle intersection implementations any zero-sequence signal can be injected to the reference modulation waves [4], [5]. The n-o potential in Fig. 1, which will be symbolized with  $v_0$ , can be freely varied. This degree of freedom is illustrated with the generalized signal diagram of Fig. 4. A properly selected zero-sequence signal can extend the volt-second linearity range of SPWM. Furthermore, it can improve the waveform quality and reduce the switching losses significantly. Recognizing these properties, many researchers have been investigating the zero-sequence signal dependency of the modulator performance, and a large number of PWM methods with unique characteristics have been reported [6]. Detailed research showed the freedom in selecting the partitioning of the two zero states

Manuscript received August 14, 1997; revised May 18, 1998. Recommended by Associate Editor, A. Goodarzi.

A. M. Hava is with Yaskawa Electric America, Inc., Waukegan, IL 60085 USA (e-mail: ahmet\_hava@yaskawa.com).

R. J. Kerkman is with Rockwell Automation/Allen Bradley, Mequon, WI 53092-0760 USA.

T. A. Lipo is with the University of Wisconsin, Madison, WI 53706-1691 USA.

Publisher Item Identifier S 0885-8993(99)00286-0.

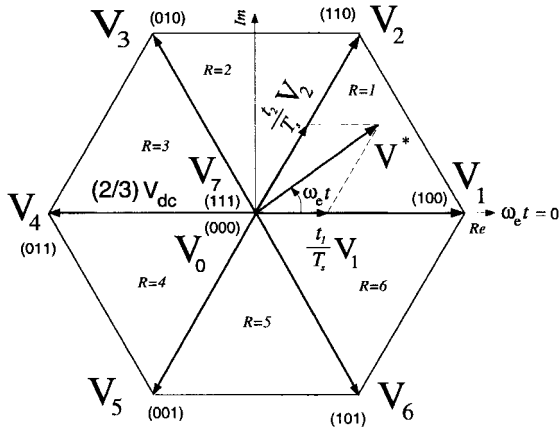


Fig. 3. The space-vector diagram illustrates the direct digital implementation principle. The upper switch states are shown in the bracket as  $(S_a+, S_b+, S_c+)$  and "1" is "on" state while "0" corresponds to "off" state.

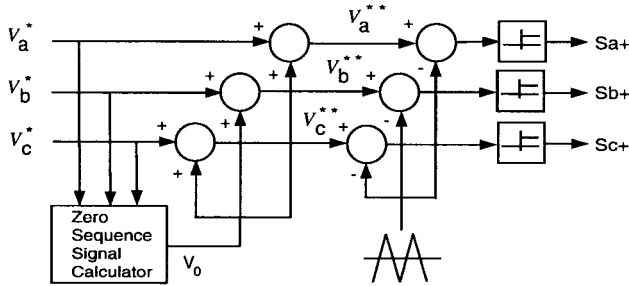


Fig. 4. The generalized signal block diagram of the triangle intersection technique-based PWM employing the zero-sequence injection principle.

"0" (000) and "7" (111) in the direct digital PWM technique is equivalent to the freedom in selecting the zero-sequence signal in the triangle intersection PWM technique [2], [7].

Although the PWM literature is rich and the technology is mature, the educational material in this field is scarce. Among the large amount of publications, several papers report and utilize powerful performance analysis tools and discuss the performance characteristics of various zero-sequence signal injection carrier-based PWM methods [8]–[10]. However, the information is often scattered and incomplete. Since the modulator characteristics are often complex, multivariable functions and the analytical formulas are nonintuitive, the PWM learning process can be discouraging, and a methodical approach is required. To understand the characteristics of various modulators, both the per-carrier cycle and per fundamental cycle behavior must be carefully studied. Therefore, establishing a methodical approach and bringing analytical tools together aids the PWM study. Furthermore, graphical methods that illustrate the performance characteristics of a modulator and compare it to other modulators would be valuable, and they would accelerate the learning process. This paper brings the analytical tools together and adds several important components to the toolbox. In addition to simplifying and accelerating the PWM learning process, the graphical illustrations and analytical tools aid the design, performance evaluation, and implementation of the modern PWM methods.

The paper first reviews the carrier-based PWM principle and summarizes the triangle intersection and space-vector approaches which lead to two different implementation techniques. After a brief review of the modern PWM methods, simple methods for generating the modulation waves of the modern triangle intersection PWM methods are described. The remainder of the paper is dedicated to the development of simple analytical tools for performance analysis. Analytical current harmonic and switching loss characteristics of various modulators are derived, graphically illustrated, and compared to distinguish the important differences. Voltage linearity is also discussed.

Since the performance characteristics of a modulator are primarily dependent on the voltage utilization level, i.e., modulation index, it is helpful to define a modulation index term at this stage. For a given dc link voltage  $V_{dc}$ , the ratio of the fundamental component magnitude of the line to neutral inverter output voltage  $V_{1m}$  to the fundamental component magnitude of the six-step mode voltage  $V_{1m6step} = (2V_{dc}/\pi)$  is termed the modulation index  $M_i$  [6]

$$M_i = \frac{V_{1m}}{V_{1m6step}}. \quad (1)$$

## II. REVIEW OF THE CARRIER-BASED PWM PRINCIPLE

Although it does not affect the inverter line to line voltage per-carrier cycle average value, the zero-sequence signal of a modulator significantly influences the switching frequency characteristics. Therefore, the per-carrier cycle (microscopic) characteristics of different modulators are important and must be modeled for detailed analysis.

As shown in Fig. 5 in the triangle intersection method, the modulation signals are compared with the triangular carrier wave and the intersection points define the switching instants. The duty cycle of each switch can be easily calculated in the following:

$$d_{S_{x+}} = \frac{1}{2} \left( 1 + \frac{v_x^{**}}{V_{dc}} \right), \quad \text{for } x \in \{a, b, c\} \quad (2)$$

$$d_{S_{x-}} = 1 - d_{S_{x+}}, \quad \text{for } x \in \{a, b, c\}. \quad (3)$$

With the modulation waveforms defined with the following cosine functions, the  $\omega_c t$  time axis of the modulation waves and complex plane reference voltage vector angle  $\omega_c t$  coincide:

$$v_a^{**} = v_a^* + v_0 = V_{1m}^* \cos(\omega_c t) + v_0 \quad (4)$$

$$v_b^{**} = v_b^* + v_0 = V_{1m}^* \cos\left(\omega_c t - \frac{2\pi}{3}\right) + v_0 \quad (5)$$

$$v_c^{**} = v_c^* + v_0 = V_{1m}^* \cos\left(\omega_c t + \frac{2\pi}{3}\right) + v_0. \quad (6)$$

For the above-defined modulation functions and  $0 \leq \omega_c t \leq (\pi/3)$ , the inverter states of the triangle intersection PWM methods are 7-2-1-0-0-1-2-7 as shown in Fig. 5. This symmetric switching sequence is superior to other sequences due to the low-harmonic-distortion characteristic. Therefore, this sequence is adopted in the direct digital methods also [2]. As

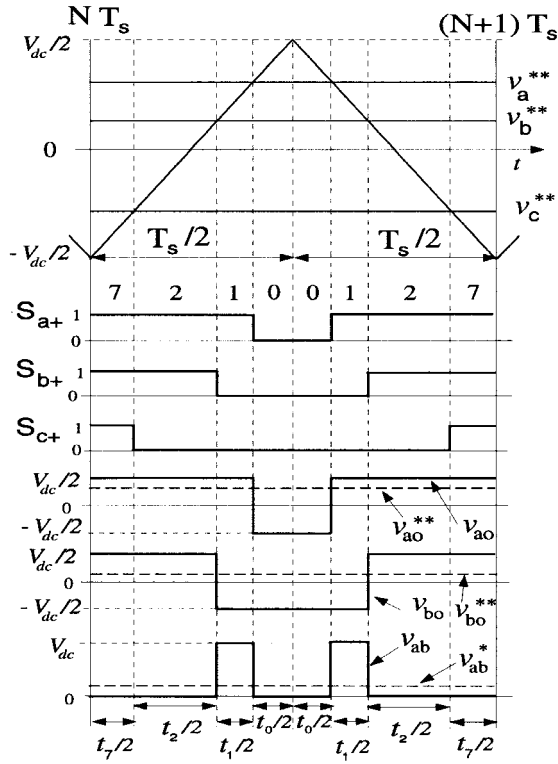


Fig. 5. The per-carrier cycle view of switch logic signals, inverter states, and VSI output voltages for  $0 \leq w_e t \leq (\pi/3)$  ( $R = 1$ ).

will be later discussed in detail, either the two “7” states at both ends or the “0” states in the middle are often omitted to further reduce the switching frequency. The zero state to be eliminated is the state which reduces the switching losses more [7]. Notice that a zero-sequence signal simultaneously shifts the three reference signals in the vertical direction and while it changes the position of the output line-to-line voltage pulses, i.e., the active inverter state time lengths, it does not affect their width. The time length of the active and zero states of the triangle intersection methods can be directly calculated from the duty-cycle information, and Fig. 5 illustrates these relations. However, in the direct digital technique, the inverter state time lengths are directly calculated employing space-vector theory, and zero-state partitioning (ZSP) is selected by the programmer.

In the space-vector approach, employing the complex variable transformation, the time domain modulation signals are translated to the complex reference voltage vector which rotates in the complex coordinates with the  $w_e t$  angular speed in the following:

$$\begin{aligned} V^* &= \frac{2}{3} (v_a^* + a v_b^* + a^2 v_c^*) \\ &= V_{1m}^* e^{j w_e t}, \quad \text{where } a = e^{j(2\pi/3)}. \end{aligned} \quad (7)$$

The complex number volt-second balance equation in the  $R$ th sector of the hexagon in Fig. 3 determines the time length of the two adjacent state active inverter states  $R$  and  $R + 1$  ( $R = 6 \rightarrow R + 1 = 1$ ) and the total zero-state time length in the following:

$$V_R t_R + V_{R+1} t_{R+1} = V^* T_s \quad (8)$$

$$t_R = \frac{2\sqrt{3}}{\pi} M_i \left[ \sin \left( R \frac{\pi}{3} - w_e t \right) \right] T_s \quad (9)$$

$$t_{R+1} = \frac{2\sqrt{3}}{\pi} M_i \left[ \sin \left( w_e t - (R - 1) \frac{\pi}{3} \right) \right] T_s \quad (10)$$

$$t_0 + t_7 = T_s - t_R - t_{R+1}. \quad (11)$$

Defined by the following, ZSP of the two inverter zero states  $\zeta_0$  and  $\zeta_7$  provides the degree of freedom in the direct digital technique [7]:

$$\zeta_0 = \frac{t_0}{t_0 + t_7} \quad (12)$$

$$\zeta_7 = 1 - \zeta_0. \quad (13)$$

In order to simplify the analytical investigations, the inverter state time lengths can be expressed in terms of per-carrier cycle or per half-carrier cycle duty cycle in the following:

$$d_R = \frac{t_R}{T_s} = \frac{t_R/2}{T_s/2}, \quad \text{for } R \in \{0, 1, \dots, 7\}. \quad (14)$$

With the degree of freedom in the triangle intersection PWM being the  $v_0$  signal, and in the direct digital technique the  $\zeta_0$  partitioning, the modern PWM methods are discussed next.

### III. MODERN PWM METHODS AND THE MAGNITUDE RULES

Although theoretically an infinite number of zero-sequence signals, and, therefore, modulation methods could be developed, the performance and simplicity constraints of practical PWM-VSI drives reduce the possibility to a small number. Over the last three decades of PWM technology evolution, about ten high-performance carrier-based PWM methods were developed, and of these only several have gained wide acceptance. Fig. 6 illustrates the modulation and zero-sequence signal waveforms of these modern triangle intersection PWM methods. In the figure, unity triangular carrier wave gain is assumed and the signals are normalized to  $V_{dc}/2$ . Therefore,  $\pm(V_{dc}/2)$  saturation limits correspond to  $\pm 1$ . In the figure, only the phase “a” modulation wave is shown, and the modulation signals of phases “b” and “c” are identical waveforms with  $120^\circ$  phase lag and lead with respect to phase “a.” The references indicated in the figure correspond to the original articles reporting these modulators.

The modulators illustrated in Fig. 6 can be separated into two groups. In the continuous PWM (CPWM) methods, the modulation waves are always within the triangle peak boundaries and within every carrier cycle triangle and modulation waves intersect, and, therefore, on and off switchings occur. In the discontinuous PWM (DPWM) methods, the modulation wave of a phase has at least one segment which is clamped to the positive or negative dc rail for at most a total of  $120^\circ$ , therefore, within such intervals the corresponding inverter leg discontinues modulation. Since no modulation implies no switching losses, the switching loss characteristics of CPWM and DPWM methods are different. Detailed studies indicated the waveform quality and linearity characteristics are also significantly different. Therefore, this classification aids in distinguishing the differences.

Of the four modern CPWM methods shown in Fig. 6, the SPWM method is the simplest modulator with limited

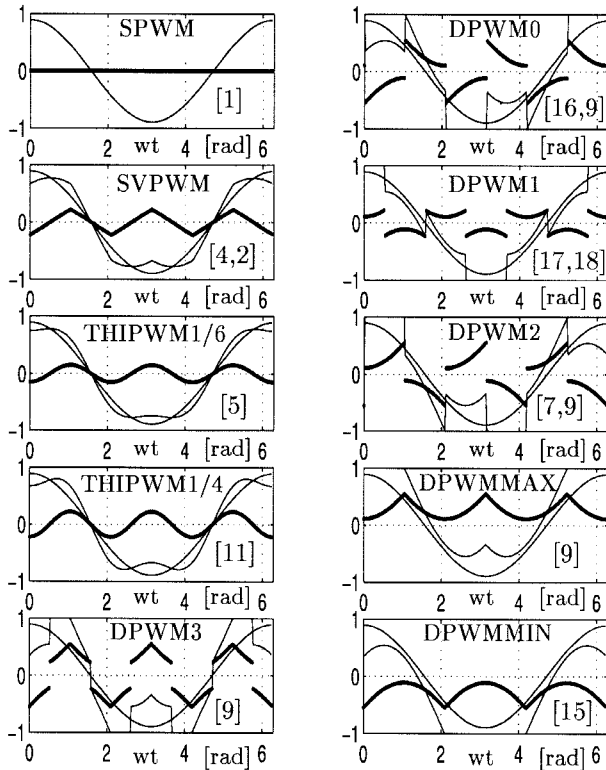


Fig. 6. Modulation waveforms of the modern PWM methods ( $M_i = 0.7$ ).

voltage linearity range and poor waveform quality in the high-modulation range. The triangle intersection implementation of the space-vector PWM (SVPWM) method and the two third harmonic injection PWM (THIPWM) methods are the other three CPWM methods which were reported in the literature. These modulators are discussed in the following.

#### A. THIPWM

Due to the simplicity of algebraically defining their zero-sequence signals, these modulators have been frequently discussed in the literature. With  $v_a^*$  defined as in (4), the zero-sequence signal of THIPWM1/6 is  $v_0 = -(V_{1m}/6)\cos 3w_e t$  [5], and for THIPWM1/4,  $v_0 = -(V_{1m}/4)\cos 3w_e t$  [11] is selected. Both methods suffer from implementation complexity because generating the  $\cos 3w_e t$  signal is difficult both with hardware and software. Trigonometric identities can be utilized to compute  $\cos 3w_e t$  from the  $\cos w_e t$  signal, however, in an on-line implementation the computational intensity (several multiplications are required) results in loss of significance by several bits, and poor resolution is obtained in signal processors with limited word length. In an off-line implementation, the functions can be precalculated and stored in the memory for on-line access. Although the THIPWM1/4 has theoretically minimum harmonic distortion, it is only slightly better than SVPWM and has narrower voltage linearity range [6], [12], [13]. With their performance being inferior to SVPWM and implementation complexity significantly higher, both THIPWM methods have academic and historical value, but little practical importance. Also note when higher order triplen harmonics are added to the THIPWM1/6 signal [such

as  $(V_{1m}/9)\cos 9w_e t$ ], the zero-sequence signal approaches a triangle and the resulting modulation signal approaches SVPWM.

#### B. SVPWM

The zero-sequence signal of SVPWM is generated by employing the minimum magnitude test which compares the magnitudes of the three reference signals and selects the signal with minimum magnitude [14]. Scaling this signal by 0.5, the zero-sequence signal of SVPWM is found. Assume  $|v_a^*| \leq |v_b^*|, |v_c^*|$ , then  $v_0 = 0.5 \times v_a^*$ . The analog implementation of SVPWM which employs a diode rectifier circuit to collect the minimum magnitude signal from the three reference signals is possibly the earliest zero-sequence signal injection PWM method reported [4]. About a decade later, this modulator reappeared in the literature with direct digital implementation [2]. Since the direct digital implementation utilized the space-vector theory, the method was named SVPWM. In addition to its implementation simplicity, the SVPWM method has superior performance characteristics and is possibly the most popular method. However, its high-modulation range performance is inferior to DPWM methods, which also employ similar magnitude rules to generate their modulation waves. In the following, the modern DPWM methods and their magnitude rules are summarized.

#### C. DPWM3

The reference signal with the intermediate magnitude defines the zero-sequence signal. Assume  $|v_b^*| \leq |v_a^*| \leq |v_c^*|$ , then  $v_0 = \text{sign}(v_a^*)(V_{dc}/2) - v_a^*$ . This method has low-harmonic distortion characteristics [12].

#### D. DPWMMAX

The reference signal with the maximum value defines the zero sequence. Assume  $v_b^* \leq v_a^* \leq v_c^*$ , then  $v_0 = (V_{dc}/2) - v_c^*$  yields and phase "c" is unmodulated [15].

#### E. DPWMMIN

The reference signal with the minimum value defines the zero sequence. Notice the DPWMMAX and DPWMMIN methods have nonuniform thermal stress on the switching devices and in DPWMMAX the upper devices have higher conduction losses than the lower, while in DPWMMIN the opposite is true.

#### F. GDPWM

DPWM0 [9], [16], DPWM1 [17], [18], and DPWM2 [7], [9] are three special cases of a generalized DPWM (GDPWM) method [19], therefore, a general study of the GDPWM method is sufficient. Fig. 7 illustrates the zero-sequence signal generation method of GDPWM. To aid the description of GDPWM, it is useful to define the modulator phase angle  $\psi$  increasing from the intersection point of the two reference modulation waves at  $w_e t = (\pi/6)$  as shown in Fig. 7. From  $\psi$  to  $\psi + (\pi/3)$ , the zero-sequence signal is the shaded signal which is equal to the difference between the saturation line

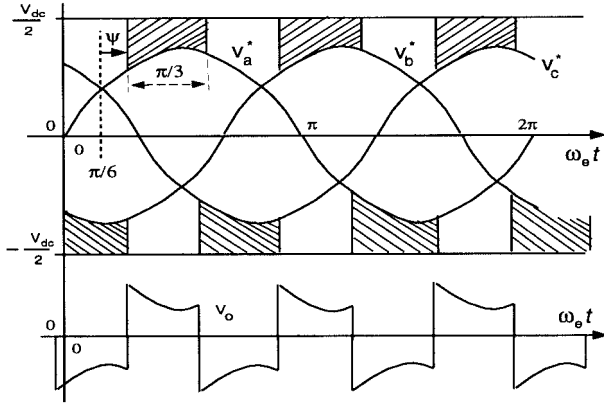


Fig. 7. Generating the GDPWM zero-sequence signal with the  $\psi$  variable.

$(V_{dc}/2)$  and the reference modulation signal which passes the maximum magnitude test. In the maximum magnitude test, all three reference modulation signals  $v_a^*$ ,  $v_b^*$ , and  $v_c^*$  are phase shifted by  $\psi - (\pi/6)$ , and of the three new signals  $v_{ax}^*$ ,  $v_{bx}^*$ , and  $v_{cx}^*$ , the one with the maximum magnitude determines the zero-sequence signal. Assume  $|v_{ax}^*| \geq |v_{bx}^*|, |v_{cx}^*|$ , then  $v_0 = (\text{sign}(v_{ax}^*)) (V_{dc}/2) - v_{ax}^*$ . Adding this zero-sequence signal to the three original modulation waves  $v_a^*$ ,  $v_b^*$ , and  $v_c^*$ , the GDPWM waves  $v_a^{**}$ ,  $v_b^{**}$ , and  $v_c^{**}$  are generated. For  $\psi = 0$  DPWM0,  $\psi = (\pi/6)$  DPWM1, and  $\psi = (\pi/3)$  DPWM2 correspond to only three operating points on the full  $\psi$  range of the modulator ( $0 \leq \psi \leq (\pi/3)$ ). Due to their superior performance characteristics, these three operating points of GDPWM have found a wide range of applications.

All the magnitude tests require a small number of computations and therefore can be easily implemented with a microcontroller or DSP. Due to the simplicity of the algorithm, it is easy to program two or more methods and on-line select a modulator in each operating region in order to obtain the highest performance [19]. Analog or digital hardware implementations of the above modulators can be easily developed by following the magnitude test computational procedures. With the exception of THIPWM and SPWM methods, all the above discussed triangle intersection PWM methods can be easily implemented in the direct digital method. Mapping the zero-state partitioning of the time domain modulation waves of Fig. 6 onto the vector space domain, the direct digital implementation equivalents can be easily obtained. Fig. 8 illustrates this equivalency and the ZSP of each method. A clear illustration of this equivalency is an important step toward simplifying the learning process.

Due to its simplicity, the magnitude test is a very effective tool for simulation, analysis, and graphic illustration of different modulation methods. For example, the simulation or DSP implementation of the SVPWM method with a direct digital technique is involved: the sector to which the voltage vector belongs has to be identified first, then the time length of each active vector must be calculated, and finally gate pulses must be generated in a correct sequence. Although it is possible to reduce the direct digital PWM algorithms, the effort does not yield as simple and intuitive a solution as the magnitude test [20]. Therefore, employing the magnitude test,

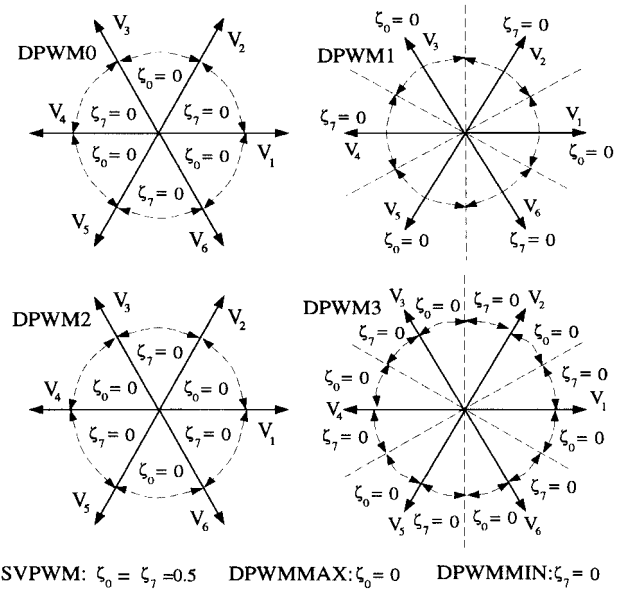


Fig. 8. Zero-state partitioning of the modern PWM methods. DPWMMIN, DPWMMAX, and SVPWM have space-invariant partitioning.

the triangle intersection PWM method is superior to the direct digital method from a simulation as well as implementation perspective. With the modulation signals generated by the magnitude test, the performance analysis follows.

#### IV. WAVEFORM QUALITY

The linear modulation range output voltage of a carrier-based PWM-VSI drive contains harmonics at the carrier frequency, at its integer multiples, and at the side bands of all these frequencies which will all be termed as “the switching frequency harmonics.” With sufficiently high-carrier frequency  $f_s$  to fundamental frequency  $f_e$  ratios ( $(f_s/f_e) > 20$ ), the low-frequency reference volt seconds are programmed accurately and the subcarrier frequency harmonic content is negligible [8]. Since modern power electronics switching devices such as insulated gate bipolar transistors (IGBT’s) and MOSFET’s typically meet this requirement, the voltage and current waveform quality of the PWM-VSI drives is determined by the switching frequency harmonics. Since they determine the switching frequency copper losses and the torque ripple of a motor load and the line current total harmonic distortion (THD) of a line-connected VSI, the switching frequency harmonic characteristics of a PWM-VSI drive are important in determining the performance. While the copper losses are measured over a fundamental cycle and therefore require a per fundamental cycle (macroscopic) rms ripple current value calculation, the peak and local stresses are properly investigated on a per-carrier cycle (microscopic) base. Therefore, first a microscopic and then a macroscopic investigation is required.

Perhaps, the most intuitive and straightforward approach for analytical investigation of the switching frequency harmonic characteristics of a PWM-VSI is the vector space approach [21], [22]. As illustrated in the vector diagram of Fig. 9, within each carrier cycle the harmonic voltage vectors  $V_{1h}$ ,  $V_{2h}$ , and  $V_{0h}$  are space and modulation index dependent. Along with the

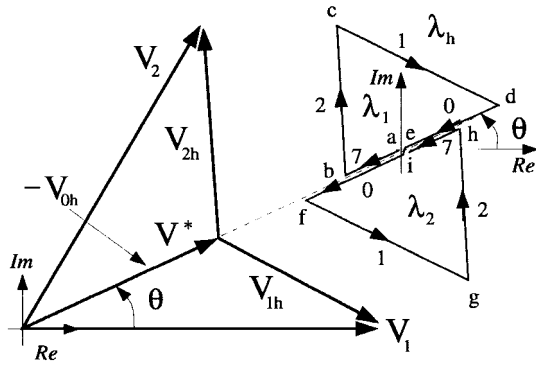


Fig. 9. Harmonic flux trajectories in the first segment of the hexagon.

harmonic voltage vectors, the duty cycle of the active inverter states and partitioning of the two zero states determine the harmonic current trajectories. Instead of the harmonic current trajectories, the conceptual harmonic flux (time integral of the harmonic voltage vector)  $\lambda_h$  trajectories can be investigated and with the assumption the load switching frequency model is an inductance [this is true in most applications due to  $(f_s/f_e) > 20$ ], the harmonic current and harmonic flux trajectories are only different in scale ( $\lambda = Li$ ). The harmonic flux in the  $N$ th carrier cycle is calculated in the following:

$$\lambda_h(M_i, \theta, V_0) = \int_{NT_s}^{(N+1)T_s} (V_k - V^*) dt. \quad (15)$$

In the above formula,  $V_k$  is the inverter output-voltage vector of the  $k$ th state, and within the carrier cycle it changes according to the selected switching sequence (7-2-1-0-1-2-7 for  $R = 1$ ). Note the harmonic flux calculation requires no load information and completely characterizes the switching frequency behavior of a modulator. Since for high  $f_s/f_e$  values the  $V^*$  term can be assumed constant within a carrier cycle and the  $V_k$  terms are constant complex numbers, the above integral can be closed-form calculated and the flux trajectories are linear over each state. Assuming its value at the beginning of the carrier cycle is zero, the harmonic flux vector crosses the origin at the center and at the end of the carrier cycle again. Therefore, (15) always assumes zero initial value. Since in the triangular intersection and direct digital PWM methods only symmetric switching sequences are generated, the integral need only be calculated in the first half of the carrier cycle, and the second half of the trajectory is exact symmetrical to the first. As illustrated in Fig. 9 for the first segment of the inverter hexagon, the harmonic flux trajectories form two triangles which may slide along the reference vector line in opposite directions with respect to the origin. It is apparent from the diagram ZSP determines the slip and affects the harmonic characteristics. Therefore, the harmonic flux trajectories of each PWM method are unique.

Calculating the harmonic flux vector for a half carrier cycle for the first region of the vector space for an arbitrary set of  $M_i, \theta$ , and ZSP ( $V_0$ ) and normalizing to  $\lambda_b$  for further simplification, the following normalized analytical harmonic flux formula  $\lambda_1(d, M_i, \theta)$  yields:

$$\lambda_b = \frac{2V_{dc} T_s}{\pi} \frac{T_s}{2} \quad (16)$$

$$\lambda_1 = \frac{\lambda_{h1}}{\lambda_b} \quad (17)$$

$$\lambda_1 = \begin{cases} -M_i e^{j\theta} d & 0 \leq d \leq d_7 \\ -\frac{\pi}{3} e^{j(\pi/3)} d_7 + \left( \frac{\pi}{3} e^{j(\pi/3)} - M_i e^{j\theta} \right) d & d_7 \leq d \leq d_7 + d_2 \\ -M_i e^{j\theta} (d_7 + d_2) + \frac{\pi}{3} e^{j(\pi/3)} d_2 & + \left( \frac{\pi}{3} - M_i e^{j\theta} \right) (d - d_7 - d_2) \\ \frac{\pi}{3} (d_1 + d_2 e^{j(\pi/3)} - M_i e^{j\theta} d) & d_7 + d_2 \leq d \leq 1 - d_0 \\ \frac{\pi}{3} & 1 - d_0 \leq d \leq 1. \end{cases} \quad (18)$$

In the second half of the carrier cycle, the harmonic flux can be calculated from the symmetry condition  $\lambda_2(d) = -\lambda_1(1-d)$ . However, in this half the inverter state duty cycles must be evaluated in the reverse sequence to the first half of the carrier cycle. The above equation can be easily programmed for any PWM method, and the space and modulation index dependency of the harmonic flux/current can be graphically illustrated. Since the inverter hexagon has sixfold symmetry, only the first segment need be investigated. The duty cycle of the active states  $d_1$  and  $d_2$  in this segment are calculated from (9), (10), and (14). In the direct digital method, the zero states are directly defined, while in the triangle intersection method the modulation waves are utilized to calculate the phase duty cycles from (2). For example, for  $R = 1$ , Fig. 5 suggests  $d_0 = d_{a-}$  and  $d_7 = d_{c+}$ .

Fig. 10 illustrates the normalized harmonic flux trajectories which are calculated from (18) for various modulators and operating conditions. To allow better visualization and clearer harmonic flux trajectory comparison, only the trajectories in the first half of a carrier cycle are illustrated in the figure and the second half is always the exact symmetric of the first. Fig. 10(a) illustrates the space dependency of the SPWM method harmonic flux. As the figure indicates, the "0" and "7" state duty cycles are not always equally split and the varying triangle shapes indicate the space dependency of the harmonic flux is strong. Fig. 10(b) compares SVPWM and THIPWM1/4 for two different angular positions. At  $w_e t = 30^\circ$ , the triangles are identical, however, at  $w_e t = 15^\circ$  the triangles have slipped. While SVPWM splits the zero states equally, the THIPWM1/4 method does slide the triangle in the direction such that the center of gravity becomes closer to the origin. Since the distance to the origin is equal to the magnitude of the harmonic flux, the trajectories which are closer to the origin result in smaller harmonic flux and the per-carrier cycle rms flux value decreases [10]. Fig. 10(c) and (d) compares SVPWM and DPWM1 and illustrates that the DPWM method always skips one of the two zero states. Therefore, the DPWM1 flux triangle is quite distant from the origin. However, increasing the carrier frequency shrinks the triangle size and brings the weight center of the triangle closer to the origin and reduces the harmonic flux. When comparing the CPWM and DPWM modulator performances, to account for the reduction in the number of per fundamental cycle switchings of the DPWM methods, a carrier frequency coefficient  $k_f$  is introduced in

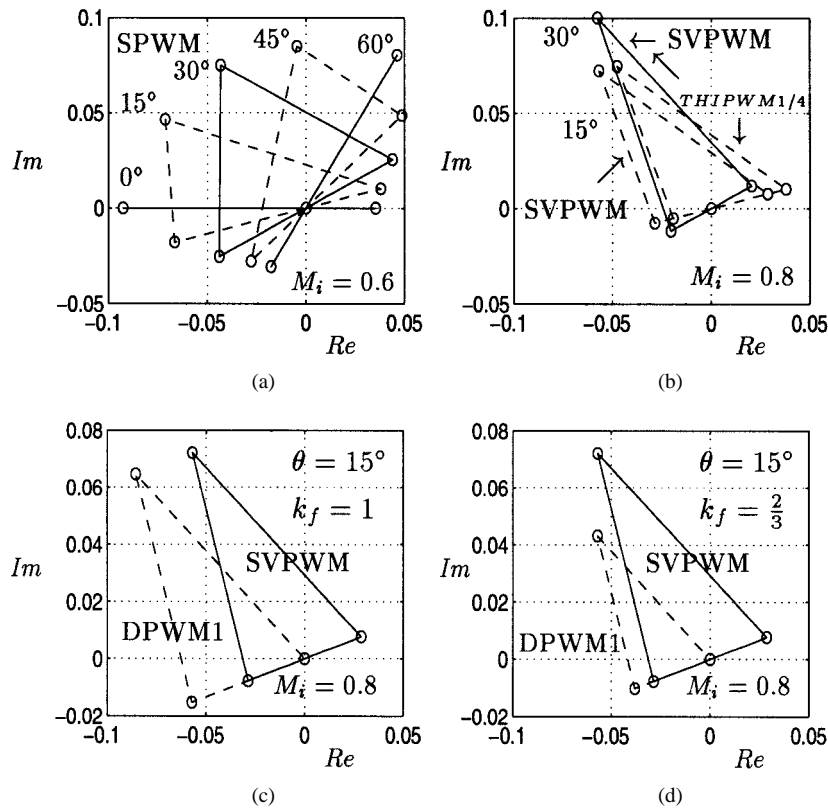


Fig. 10. The switching frequency harmonic flux trajectories of various PWM methods. (a) SPWM, (b) SVPWM and THIPWM1/4 compared for  $w_e t = 15^\circ$  and  $w_e t = 30^\circ$  values, (c) SVPWM and DPWM1 compared ( $k_f = 1$ ), and (d) SVPWM and DPWM1 for  $k_f = \frac{2}{3}$ .

the following:

$$k_f = \frac{f_{s\text{CPWM}}}{f_{s\text{DPWM}}}. \quad (19)$$

Employing (18), the per-carrier cycle rms value of the harmonic flux  $\lambda_{1\text{rms}}$  can be closed-form calculated. Since the first and the second halves of the trajectory have the same rms value due to symmetry, calculating only the first is sufficient. Involved calculations yield the following  $M_i$  and duty-cycle-dependent formula:

$$\lambda_{1\text{rms}}^2 = \int_0^1 \lambda_1^2 dd = \lambda_{11}^2 + \lambda_{12}^2 + \lambda_{13}^2 \quad (20)$$

$$\lambda_{11}^2 = \frac{\pi^2}{18} M_i^2 \left( \frac{1}{3} + d_0^2 + d_1^2 - d_0 - d_1 + 2d_0d_1 \right) \quad (21)$$

$$\lambda_{12}^2 = \frac{\pi^4}{72} \left[ \frac{1}{3} (2d_1^3 - 4d_2^3 - 4d_1^4 + 2d_2^4 + 7d_1d_2^3 - 2d_2d_1^3) + d_1^2d_2^2 \right] \quad (22)$$

$$\lambda_{13}^2 = \frac{\pi^4}{72} [-d_1d_2^2 + d_0(d_1d_2^2 - 2d_1^3 + 2d_2^3 - d_1^2d_2)]. \quad (23)$$

Employing the above formula, the  $\theta$  and  $M_i$  dependency of  $\lambda_{1\text{rms}}^2$  of various PWM methods can be easily computed and graphically illustrated. Figs. 11 and 12 compare the rms harmonic flux characteristics of the modern methods for two modulation index values for  $k_f = 1$ . The figures indicate the CPWM methods have lower harmonic distortion than the DPWM methods, and the difference is more pronounced at

low  $M_i$ . The THIPWM1/4 method, which is the minimum harmonic distortion method—the optimality condition can be verified by searching the minimum of (20) with respect to  $d_0$  [12]—has only slightly less distortion than SVPWM and only near the  $15^\circ$  and  $45^\circ$  range. Since the DPWM methods have a discrete ZSP (zero or one) and within certain segments ZSP of various DPWM methods is the same (see Fig. 8). Therefore, calculating the rms harmonic flux of DPWM methods is a relatively simple task and  $\zeta_0 = 0$  for A and  $\zeta_0 = 1$  for C are the only two functions required to determine the rms flux curves of all DPWM methods. The overall comparison indicates SVPWM provides superior performance in the low-modulation range, however, as  $M_i$  increases, the performance of DPWM methods significantly improves and becomes comparable to SVPWM.

As Figs. 11 and 12 clearly illustrate the strong space dependency of the per-carrier cycle rms harmonic distortion characteristics of all the modern PWM methods, it becomes apparent that performance can be gained by modulating the carrier frequency. If the carrier frequency is methodically increased at the high-rms harmonic flux intervals and reduced at the low-harmonic rms flux intervals, then the overall harmonic distortion characteristics can be reduced [23]. Provided the inverter average switching frequency is maintained constant, the switching loss characteristics are not affected by the frequency modulation and performance gain without efficiency reduction becomes possible. Since the per-carrier cycle rms harmonic flux characteristics are strongly influenced by the modulator zero-sequence signals and they repeat at

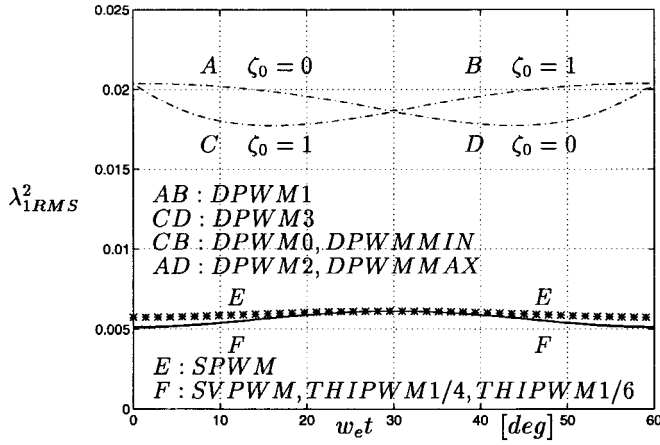


Fig. 11. The space dependency of the per-carrier cycle normalized rms harmonic flux of the modern PWM methods for  $M_i = 0.4$  and  $k_f = 1$ .

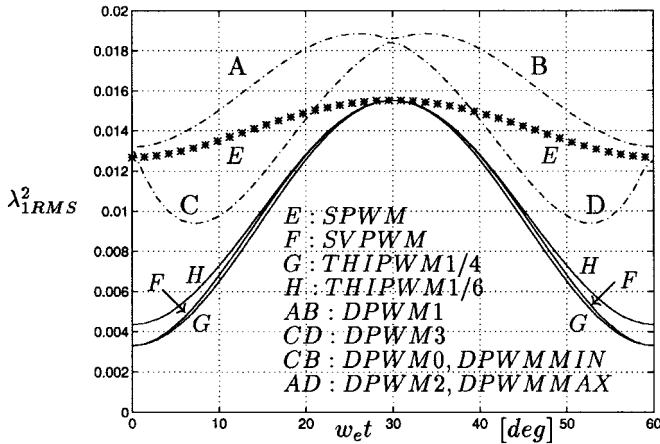


Fig. 12. The space dependency of the per-carrier cycle normalized rms harmonic flux of the modern PWM methods for  $M_i = 0.78$  and  $k_f = 1$ .

the same frequency, the zero-sequence signals can aid in establishing simple frequency modulation signals and simple implementations result [13]. Since the frequency modulation techniques are most beneficial to modulators with strongly space-dependent rms harmonic flux characteristics, CPWM methods are more suitable candidates than DPWM methods for this approach. In addition to reducing the rms harmonic distortion and the peak ripple current, the frequency modulation techniques also flatten the inverter output-voltage/current harmonic spectrum. Therefore, they are suitable for high-power-quality applications that require a flat harmonic spectrum with no dominant harmonic content.

Since it determines the waveform quality and harmonic losses, the per fundamental cycle rms value  $\lambda_{1\text{frms}}$  of the harmonic flux is the most important performance characteristic of a modulator. Since the  $\lambda_{1\text{frms}}^2$  characteristics of the modern PWM methods have sixfold space symmetry, the per fundamental cycle (per  $60^\circ$  in space) rms harmonic flux value can be calculated in the following:

$$\lambda_{1\text{frms}}^2 = \frac{3}{\pi} \int_0^{\pi/3} \lambda_{1\text{frms}}^2 d\theta. \quad (24)$$

For each modulator, the above integral yields a polynomial function of  $M_i$  with unique coefficients, and it can be written in the following  $M_i$ -dependent harmonic distortion function (HDF) formula:

$$\lambda_{1\text{frms}}^2 = \frac{\pi^2}{288} \quad \text{HDF} = \frac{\pi^2}{288} (a_m M_i^2 + b_m M_i^3 + c_m M_i^4). \quad (25)$$

Calculating  $a_m$ ,  $b_m$ , and  $c_m$  of each modulator involves significant algebraic manipulations. The resulting HDF functions of the discussed modulators are summarized in the following:

$$\begin{aligned} \text{HDF}_{\text{SPWM}} &= \frac{3}{2} \left( \frac{4}{\pi} M_i \right)^2 - \frac{4\sqrt{3}}{\pi} \left( \frac{4}{\pi} M_i \right)^3 \\ &+ \left( \frac{9}{8} \right) \left( \frac{4}{\pi} M_i \right)^4 \end{aligned} \quad (26)$$

$$\begin{aligned} \text{HDF}_{\text{THIPWM6}} &= \frac{3}{2} \left( \frac{4}{\pi} M_i \right)^2 - \frac{4\sqrt{3}}{\pi} \left( \frac{4}{\pi} M_i \right)^3 \\ &+ \left( \frac{4}{\pi} M_i \right)^4 \end{aligned} \quad (27)$$

$$\begin{aligned} \text{HDF}_{\text{THIPWM4}} &= \frac{3}{2} \left( \frac{4}{\pi} M_i \right)^2 - \frac{4\sqrt{3}}{\pi} \left( \frac{4}{\pi} M_i \right)^3 \\ &+ \left( \frac{63}{64} \right) \left( \frac{4}{\pi} M_i \right)^4 \end{aligned} \quad (28)$$

$$\begin{aligned} \text{HDF}_{\text{SVPWM}} &= \frac{3}{2} \left( \frac{4}{\pi} M_i \right)^2 - \frac{4\sqrt{3}}{\pi} \left( \frac{4}{\pi} M_i \right)^3 \\ &+ \left( \frac{27}{16} - \frac{81\sqrt{3}}{64\pi} \right) \left( \frac{4}{\pi} M_i \right)^4. \end{aligned} \quad (29)$$

As was shown in Figs. 11 and 12, the harmonic flux of DPWM methods consists of a combination of the A, B, C, and D segments. A and B yield equivalent distortion and so do C and D. Therefore, calculating the HDF of A-B ( $\text{HDF}_{\text{DMAX}}$ ) and C-D ( $\text{HDF}_{\text{DMIN}}$ ) is sufficient in determining the performance of all the DPWM methods discussed. The results are as follows:

$$\begin{aligned} \text{HDF}_{\text{DMAX}} &= 6 \left( \frac{4}{\pi} M_i \right)^2 - \left( \frac{8\sqrt{3} + 45}{2\pi} \right) \left( \frac{4}{\pi} M_i \right)^3 \\ &+ \left( \frac{27}{8} + \frac{27\sqrt{3}}{32\pi} \right) \left( \frac{4}{\pi} M_i \right)^4 \end{aligned} \quad (30)$$

$$\begin{aligned} \text{HDF}_{\text{DMIN}} &= 6 \left( \frac{4}{\pi} M_i \right)^2 + \left( \frac{45 - 62\sqrt{3}}{2\pi} \right) \left( \frac{4}{\pi} M_i \right)^3 \\ &+ \left( \frac{27}{8} + \frac{27\sqrt{3}}{16\pi} \right) \left( \frac{4}{\pi} M_i \right)^4. \end{aligned} \quad (31)$$

For the same carrier frequency, the DPWM methods have fewer switchings per fundamental cycle than the CPWM methods, therefore, to illustrate the carrier frequency effect,  $k_f$  is included in the HDF formulas of the DPWM methods

$$\text{HDF}_{\text{DPWM1}} = k_f^2 \times \text{HDF}_{\text{DMAX}} \quad (32)$$

$$\text{HDF}_{\text{DPWM3}} = k_f^2 \times \text{HDF}_{\text{DMIN}} \quad (33)$$

$$\text{HDF}_{\text{DPWM0}} = k_f^2 \times 0.5 \times (\text{HDF}_{\text{DMIN}} + \text{HDF}_{\text{DMAX}}) \quad (34)$$

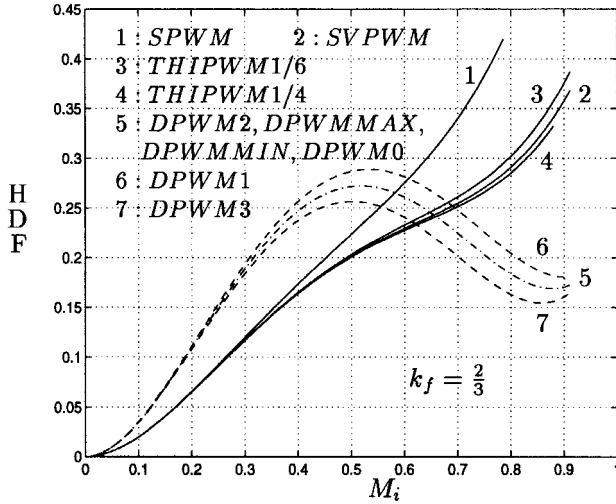


Fig. 13. HDF =  $f(M_i)$  curves in the linear modulation range under constant inverter average switching frequency condition.

$$\begin{aligned} \text{HDF}_{\text{DPWM2}} &= \text{HDF}_{\text{DPWMMIN}} = \text{HDF}_{\text{DPWMMAX}} \\ &= \text{HDF}_{\text{DPWM0}}. \end{aligned} \quad (35)$$

The relation between HDF and the per phase harmonic current rms value  $I_h$  for a load with a transient inductance  $L_\sigma$ , which can be utilized in calculating the harmonic copper losses, is as follows:

$$I_{xh}^2 = \left( \frac{V_{dc}}{24L_\sigma f_s} \right)^2 \times \text{HDF}(M_i), \quad \text{for } x \in \{a, b, c\}. \quad (36)$$

Fig. 13 shows the HDF curves of all the discussed PWM methods. In the very low-modulation index range, all CPWM methods have practically equal HDF which is superior to all DPWM methods. As the modulation index increases, the SPWM performance rapidly degrades while the remaining CPWM methods maintain low HDF over a wide modulation range. The figure indicates the THIPWM1/4 performance is only slightly better than SVPWM, and the difference is less noticeable than the local differences shown in Figs. 10 and 12. In the high-modulation range, the DPWM methods are superior to SVPWM (Fig. 13) and the intersection point of the DPWM method of choice and SVPWM defines the optimal transition point. Although in the high-modulation range the DPWM3 method has less HDF than the other DPWM methods, the improvement is marginal and the modulator selection criteria can be based on the switching loss characteristics and voltage linearity characteristics which are stronger functions of the DPWM methods. The HDF of GDPWM method is  $\psi$  dependent and varies between curves 5 and 6 of Fig. 13. Its HDF can be approximated with the average value of (32) and (34)

$$\text{HDF}_{\text{GDPWM}} \approx k_f^2 \times 0.25 \times (\text{HDF}_{\text{DMIN}} + 3\text{HDF}_{\text{DMAX}}). \quad (37)$$

Since the HDF of each PWM method is unique, the switching frequency harmonic spectrum of each method is also unique. Since the DPWM methods have two fewer switchings per-carrier cycle than CPWM methods, the side-band

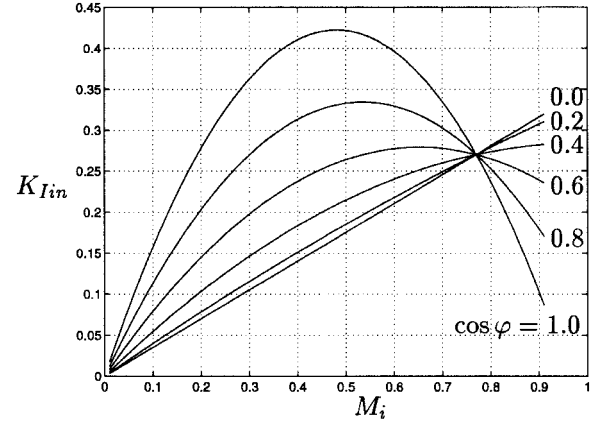


Fig. 14. Normalized inverter input harmonic current rms value characteristics  $K_{In} = f(M_i)$  of PWM-VSI for  $\cos \varphi$  as parameter.

harmonics of the DPWM methods are wider and larger in magnitude. Calculating the individual harmonics and the peak ripple current is involved and will be omitted herein. Having illustrated the superior high-modulation range waveform quality characteristics of the DPWM methods over SVPWM, in the next section the switching losses of DPWM methods will be characterized to aid an intelligent modulator choice. Following a brief section on the inverter input current harmonics, the switching losses of the DPWM methods will be analytically modeled and their performance evaluated.

## V. INVERTER INPUT CURRENT HARMONICS

The dc link input current of a PWM inverter  $I_{in}$  consists of the dc average value  $I_{dc}$  which corresponds to the average power transfer to the load and switching frequency component  $I_{inh}$  which is due to PWM switching. Since during the zero states the dc link is decoupled from the ac load, the rms value of the ripple current  $I_{inh\text{rms}}$ , which is required in dc link capacitor design and loss calculations, is independent of the zero-sequence signal and therefore of the modulator type. Since the duty cycles of the inverter active states are independent of the carrier frequency,  $I_{inh\text{rms}}$  is also independent of the carrier frequency. Similar to the inverter output current harmonic rms current calculation,  $I_{inh\text{rms}}$  can also be easily calculated by establishing a per-carrier cycle rms value formula and evaluating it over an inverter segment [21]. The calculation yields the following  $M_i$ , load power factor ( $\cos \varphi$ ), and load current fundamental component rms value ( $I_{1\text{rms}}$ ) dependent dc link current ripple factor  $K_{In}$  formula:

$$K_{In} = \frac{I_{inh\text{rms}}^2}{I_{1\text{rms}}^2} = \frac{2\sqrt{3}}{\pi^2} M_i + \left( \frac{8\sqrt{3}}{\pi^2} - \frac{18}{\pi^2} M_i \right) M_i \cos^2 \varphi. \quad (38)$$

Fig. 14 illustrates the  $M_i$  and  $\cos \varphi$  dependency of the  $K_{In}$  factor. The maximum ripple occurs at  $\cos \varphi = 1$  and at  $M_i = (5\sqrt{3}/18) \approx 0.48$  (a reasonable design point for capacitor sizing), and the ripple is independent of  $\cos \varphi$  at  $M_i = (8/\sqrt{3}/18) \approx 0.77$ .

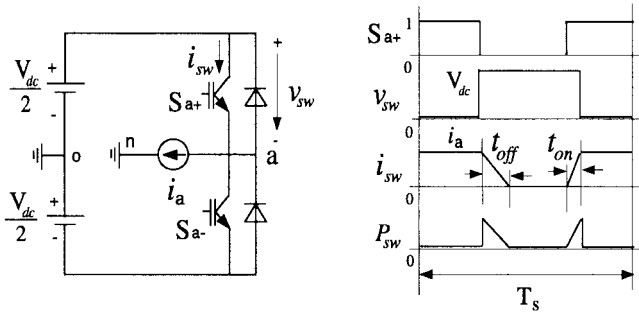


Fig. 15. The inverter per phase model and per-carrier cycle switching loss diagram under linear commutation.

## VI. SWITCHING LOSSES

The switching losses of a PWM-VSI drive are load-current dependent and increase with the current magnitude (approximately linearly). With CPWM methods, all the three-phase currents are commutated within each carrier cycle of a full fundamental cycle. Therefore, for all CPWM methods, the switching losses are the same and independent of the load current phase angle. With DPWM methods, however, the switching losses are significantly influenced by the modulation method and load power factor angle. Because DPWM methods cease to switch each switch for a total of  $120^\circ$  per fundamental cycle and the location of the unmodulated segments with respect to the modulation wave fundamental component phase is modulator-type dependent. Therefore, the load power factor and the modulation method together determine the time interval that the load current is not commutated. Since the switching losses are strongly dependent on and increase with the magnitude of the commutating phase current, selecting a DPWM method with reduced switching losses can significantly contribute to the performance of the drive. Therefore, it is necessary to characterize and compare the switching losses of DPWM methods.

Assuming the inverter switching devices have linear current turn-on and turn-off characteristics with respect to time and accounting only for the fundamental component of the load current, the switching losses of a PWM-VSI drive can be analytically modeled [9]. Shown in Fig. 15, the single-phase inverter model and the switching voltage/current diagram aid calculating the switching losses. Deriving the local (per-carrier cycle) switching loss formula and calculating its average value over the fundamental cycle, the per fundamental cycle inverter per device switching loss  $P_{swave}$  can be calculated as follows:

$$P_{swave} = \frac{1}{2\pi} \frac{V_{dc}(t_{on} + t_{off})}{2T_s} \int_0^{2\pi} f_i(\theta) d\theta. \quad (39)$$

In the above formula,  $t_{on}$  and  $t_{off}$  variables represent the turn-on and turn-off times of the switching devices and  $f_i(\theta)$  is the switching current function. The switching current function  $f_i(\theta)$  equals zero in the intervals where modulation ceases and the absolute value of the corresponding phase current value elsewhere. As a result, the phase current power factor angle  $\varphi$  enters the formula as the integral boundary term and  $\varphi$  dependent switching loss formula yields. Normalizing  $P_{swave}$  to  $P_o$ , the switching loss value under CPWM condition (which

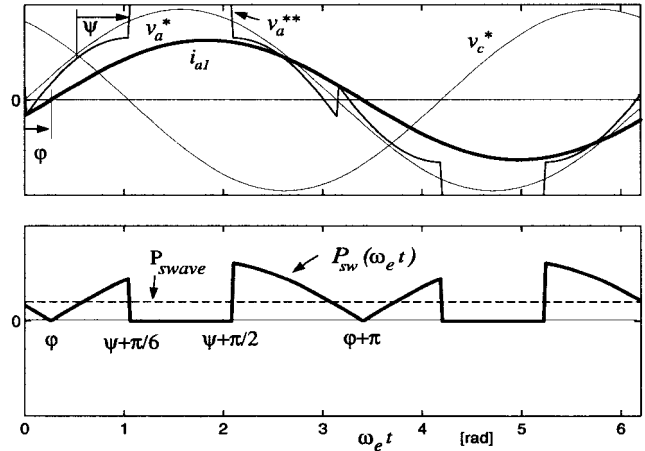


Fig. 16. The average switching losses of GDPWM,  $P_{swave} = f(\psi, \varphi)$ .

is  $\varphi$  independent), the switching loss function (SLF) of a modulator can be found

$$P_o = \frac{V_{dc} I_{max}}{\pi T_s} \times (t_{on} + t_{off}) \quad (40)$$

$$SLF = \frac{P_{swave}}{P_o}. \quad (41)$$

In (40), the variable  $I_{max}$  represents the load current fundamental component maximum value. By the definition of (41), the SLF of CPWM methods is unity. The SLF of the DPWM methods can be easily calculated from the current switching function. Fig. 16 shows the  $\psi$  and  $\varphi$  dependent switching loss function waveforms of GDPWM. Applying the procedure to GDPWM yields the following SLF [13]:

$$SLF_{GDPWM} = \begin{cases} \frac{\sqrt{3}}{2} \cos\left(\frac{4\pi}{3} + \psi - \varphi\right) & -\frac{\pi}{2} \leq \varphi \leq -\frac{\pi}{2} + \psi \\ 1 - \frac{1}{2} \sin\left(\frac{\pi}{3} + \psi - \varphi\right) & -\frac{\pi}{2} + \psi \leq \varphi \leq \frac{\pi}{6} + \psi \\ \frac{\sqrt{3}}{2} \cos\left(\frac{\pi}{3} + \psi - \varphi\right) & \frac{\pi}{6} + \psi \leq \varphi \leq \frac{\pi}{2}. \end{cases} \quad (42)$$

The SLF function of the DPWM0, DPWM1, and DPWM2 can be easily evaluated from (42) by substituting  $\psi = 0$ ,  $\psi = (\pi/6)$ , and  $\psi = (\pi/3)$ . The SLF of the remaining DPWM methods are as follows:

$$SLF_{DPWMMIN} = \begin{cases} \frac{1}{2} - \frac{1}{4} \sin \varphi & -\frac{\pi}{2} \leq \varphi \leq -\frac{\pi}{6} \\ 1 - \frac{\sqrt{3}}{4} \cos \varphi & -\frac{\pi}{6} \leq \varphi \leq \frac{\pi}{6} \\ \frac{1}{2} + \frac{1}{4} \sin \varphi & \frac{\pi}{6} \leq \varphi \leq \frac{\pi}{2} \end{cases} \quad (43)$$

$$SLF_{DPWMMAX} = SLF_{DPWMMIN} \quad (44)$$

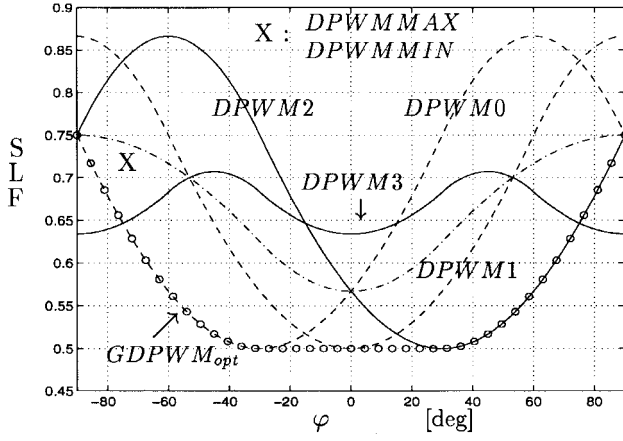


Fig. 17. SLF =  $f(\varphi)$  characteristics of the popular DPWM methods under fixed carrier frequency constraint ( $SLF_{DPWM} = 1$ ).

$$SLF_{DPWM3} = \begin{cases} 1 + 0.5(\sqrt{3} - 1) \sin \varphi & -\frac{\pi}{2} \leq \varphi \leq -\frac{\pi}{3} \\ 0.5(\cos \varphi - \sin \varphi) & -\frac{\pi}{3} \leq \varphi \leq -\frac{\pi}{6} \\ 1 - 0.5(\sqrt{3} - 1) \cos \varphi & -\frac{\pi}{6} \leq \varphi \leq \frac{\pi}{6} \\ 0.5(\cos \varphi + \sin \varphi) & \frac{\pi}{6} \leq \varphi \leq \frac{\pi}{3} \\ 1 - 0.5(\sqrt{3} - 1) \sin \varphi & \frac{\pi}{3} \leq \varphi \leq \frac{\pi}{2} \end{cases} \quad (45)$$

Although the absolute switching loss values obtained from (39) may have limited accuracy due to unmodeled switching device characteristics, the relative switching losses which are represented with the SLF function are always predicted with higher accuracy. Since the SLF derivation assumes the same device characteristics both in  $P_{swave}$  and  $P_o$ , the error direction is the same in both terms and therefore the relative error is reduced. The SLF functions are powerful analytical tools for evaluating and comparing the switching losses of various DPWM methods.

Fig. 17 shows the SLF characteristics of the modern DPWM methods along with the minimum SLF solution the GDPWM method yields. The optimal solution of GDPWM is obtained by selecting  $\psi = (\pi/6) + \varphi$  for  $-(\pi/6) \leq \varphi \leq (\pi/6)$  [19]. Outside this range, the modulator phase angle must be held at the boundary value of  $\psi = (\pi/3)$  for positive  $\varphi$  (DPWM2) and at the value of  $\psi = 0$  for negative  $\varphi$  (DPWM0) so that the GDPWM voltage linearity is retained. Note that outside the  $-(5\pi/12) \leq \varphi \leq (5\pi/12)$  range DPWM3 yields minimum switching losses. As Fig. 17 indicates, the switching losses of DPWM methods strongly depend on  $\varphi$  and can be reduced to 50% of the CPWM methods. Therefore, the SLF characteristics are as important as the HDF characteristics in determining the performance of a modulator.

## VII. OVERMODULATION AND VOLTAGE GAIN

In the triangle intersection PWM technique, when the modulation wave magnitude becomes larger than the triangular

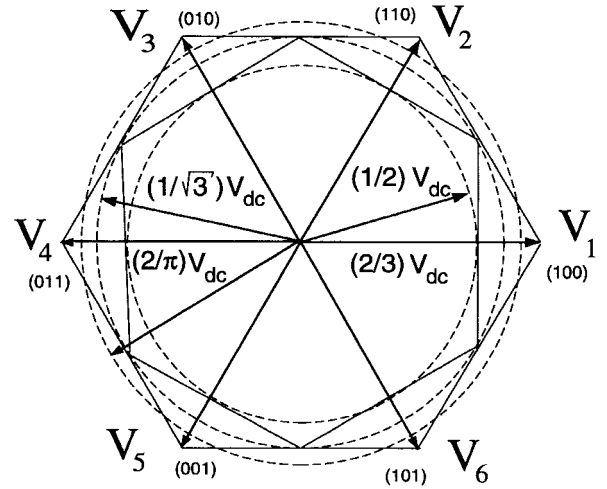


Fig. 18. Vector space illustration of the PWM inverter voltage linearity limits.

carrier wave peak value  $\pm(V_{dc}/2)$ , the inverter ceases to match the reference per-carrier cycle volt seconds and a nonlinear reference output-voltage relation results within certain intervals. SPWM's linear modulation range ends at  $V_{1m}^* = (V_{dc}/2)$ , i.e., a modulation index of  $M_{LSPWM} = (\pi/4) \approx 0.785$ . Injecting a zero-sequence signal to the SPWM signal can flatten and contain the modulation wave within  $\pm(V_{dc}/2)$  such that the linearity range is extended to at most  $M_{Lmax} = (\pi/2\sqrt{3}) \approx 0.907$  which is the theoretical inverter linearity limit [4], [5], [13]. With the exception of THIPWM1/4 which loses linearity at  $M_{LTHIPWM1/4} = (3\sqrt{3}/7\sqrt{7})\pi \approx 0.881$ , all the discussed zero-sequence injection PWM methods are linear until  $M_{Lmax}$ .

In the direct digital technique, when the reference voltage vector falls outside the modulator linearity region, (11) yields  $t_0 + t_7 \leq 0$ , indicating the reference volt seconds cannot be matched by the inverter, and a volt-second error is inevitable. Shown in Fig. 18, the complex plane linearity boundaries of the modern modulators correspond to hexagons. The outer hexagon is the inverter theoretical linearity limit and with the exception of SPWM, THIPWM1/4, and THIPWM1/6, all the discussed PWM methods (direct digital or triangle intersection based) are linear inside the hexagon. The SPWM linearity limit is shown in the same diagram with the internal hexagon. The per fundamental component linearity boundaries of these modulators are illustrated with circles which touch the inner boundaries of the hexagons. Fig. 19 illustrates the per-carrier cycle voltage limits of all the modern PWM methods in detail. The THIPWM1/6 method has elliptic boundaries, while the THIPWM1/4 linearity boundaries resemble the shape of a star with 12 edges [13].

The region starting from the end of the linear modulation region of a modulator until the six-step operating point ( $M_i = 1$ ) is called the overmodulation region. All the PWM-VSI drives experience performance degradation in the overmodulation region and operating in this region is often problematic [13], [24]–[27]. The output-voltage waveform quality degrades (subcarrier frequency harmonics are generated), and the voltage becomes increasingly smaller

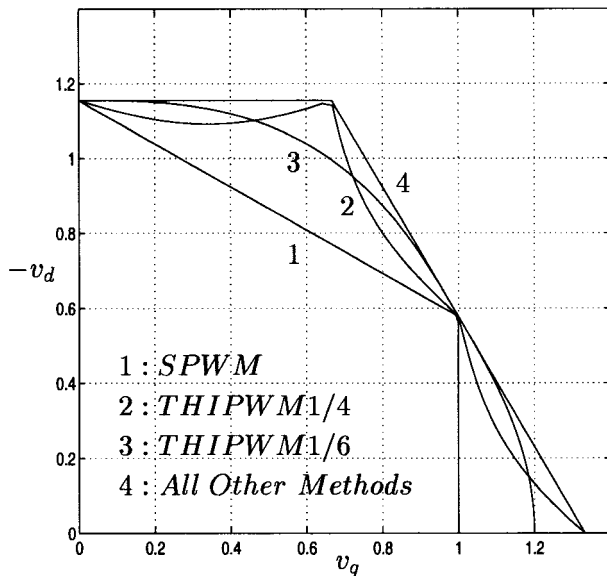


Fig. 19. Vector space illustration of the modulator per-carrier cycle voltage linearity limits. All voltage vectors are normalized to  $V_{dc}/2$ .

than the reference. However, the overmodulation issues of the closed-loop (current-controlled) PWM-VSI drives with high-dynamic performance requirements and the open-loop ( $(V/f) = \text{const.}$ ) drives are significantly different [13], [26].

In high-dynamic performance applications, the per-carrier cycle volt-second errors should be minimized to manipulate a dynamic condition as fast as possible [25]. Therefore, the reference output-voltage vector relations influence the dynamic overmodulation performance of a drive. Reference [25] studies the direct digital PWM issues while [28] analytically models the triangle intersection PWM modulator dynamic overmodulation characteristics in detail.

In open-loop drives, the dynamic performance requirements are not stringent, however, high per fundamental cycle (steady state) performance must be obtained. Correct per fundamental cycle volt seconds and low-harmonic distortion is desirable. However, due to saturation, the output-voltage fundamental component is smaller than the reference, and as the modulation index increases, the voltage gain rapidly decreases and the subcarrier frequency harmonic content rapidly increases. Both the per fundamental component voltage gain and the subcarrier frequency harmonic characteristics of each modulator are unique. Both characteristics of the triangle intersection [13], [26], [27] and direct digital PWM [24] implementations have been recently investigated in detail and will not be pursued in this paper.

The dynamic and steady-state overmodulation analytical tools established in the suggested literature are complementary parts of the PWM toolbox developed in this paper and could aid the PWM education as well as the practical design and performance evaluation.

### VIII. CONCLUSIONS

Simple and powerful analytical and graphical carrier-based PWM tools have been developed. These tools were utilized to illustrate and compare the performance characteristics of

various PWM methods. The switching loss and waveform quality comparisons indicate SVPWM at low modulation and DPWM methods at the high-modulation range have superior performance. The tools and graphics aid the modulator selection and PWM inverter design process. The magnitude test is an elegant method for generating the modulation waveforms fast and accurately by digital hardware/software or analog hardware. The analytical methods are also helpful in generating graphics of the microscopic current ripple characteristics and illustrating the performance characteristics and the difference between various modulators. Therefore, they aid visual learning. As a result, the paper helps the PWM learning and design experience become simple and intuitive.

### REFERENCES

- [1] A. Schöning and H. Stemmler, "Static frequency changers with subharmonic control in conjunction with reversible variable speed ac drives," *Brown Boveri Rev.*, Sept. 1964, pp. 555-577.
- [2] H. Van Der Broeck, H. Skudelny, and G. Stanke, "Analysis and realization of a pulse width modulator based on voltage space vectors," in *IEEE-IAS Conf. Rec.*, 1986, pp. 244-251.
- [3] G. Pfaff, A. Weschta, and A. Wick, "Design and experimental results of a brushless ac servo-drive," in *IEEE-Industrial Application Soc. Conf. Rec.*, San Francisco, CA, 1982, pp. 692-697.
- [4] K. G. King, "A three phase transistor class-b driver inverter with sinewave output and high efficiency," in *Inst. Elec. Eng. Conf.*, 1974, pp. 204-209.
- [5] G. Buja and G. Indri, "Improvement of pulse width modulation techniques," *Archiv für Elektrotechnik*, vol. 57, pp. 281-289, 1975.
- [6] J. Holtz, "Pulsewidth modulation for electronic power conversion," *Proc. IEEE*, vol. 8, pp. 1194-1214, Aug. 1994.
- [7] S. Ogasawara, H. Akagi, and A. Nabae, "A novel PWM scheme of voltage source inverter based on space vector theory," in *European Power Electron. Conf. Rec.*, Aachen, Germany, 1989, pp. 1197-1202.
- [8] H. W. Van Der Broeck, "Analysis of the harmonics in voltage fed inverter drives caused by PWM schemes with discontinuous switching operation," in *European Power Electron. Conf. Rec.*, 1991, pp. 261-266.
- [9] J. W. Kolar, H. Ertl, and F. C. Zach, "Influence of the modulation method on the conduction and switching losses of a PWM converter system," *IEEE Trans. Ind. Applicat.*, vol. 27, pp. 1063-1075, Nov./Dec. 1991.
- [10] ———, "Minimizing the current harmonics rms value of three-phase PWM converter systems by optimal and suboptimal transition between continuous and discontinuous modulation," in *IEEE-Power Electronics Specialists. Conf. Rec.*, San Antonio, TX, 1991, pp. 372-381.
- [11] S. R. Bowes and A. Midoun, "Suboptimal switching strategies for microprocessor controlled PWM inverter drives," *Proc. Inst. Elect. Eng.*, vol. 132, pt. B, pp. 133-148, May 1985.
- [12] K. W. Kolar, H. Ertl, and F. C. Zach, "Minimization of the harmonic rms content of the mains current of a PWM converter system based on the solution of an extreme value problem," in *ICHPC Conf. Rec.*, Budapest, Hungary, 1990, pp. 234-243.
- [13] A. M. Hava, "Carrier based PWM-VSI drives in the overmodulation region," Ph.D. dissertation, Univ. Wisconsin, Madison, 1998.
- [14] L. J. Garces, "Current control of field oriented ac induction motor drives," in *IEEE Tutorial: Microprocessor Control of Motor Drives and Power Converters*, 1993, pp. 5-1-5-46.
- [15] K. Taniguchi, Y. Ogino, and H. Irie, "PWM technique for power MOSFET inverter," *IEEE Trans. Power Electron.*, July 1988, pp. 328-334.
- [16] T. Kenjo, *Power Electronics for the Microprocessor Age*. Oxford, U.K.: Oxford Univ. Press, 1990.
- [17] J. Schrömer, "Bezugsspannung zur umrichtersteuerung," in *ETZ-b, Bd. 27*, pp. 151-152, 1976.
- [18] M. Depenbrock, "Pulse width control of a 3-phase inverter with non-sinusoidal phase voltages," in *IEEE-ISPC Conf. Rec.*, pp. 399-403, 1977.
- [19] A. M. Hava, R. J. Kerkman, and T. A. Lipo, "A high performance generalized discontinuous PWM algorithm," in *IEEE-APEC Conf. Rec.*, Atlanta, GA, 1997, pp. 886-894.
- [20] J.-S. Kim and S.-K. Sul, "A novel voltage modulation technique of the space vector PWM," in *IPEC-Yokohama Conf. Rec.*, Yokohama, Japan, 1995, pp. 742-747.

- [21] J. W. Kolar, H. Ertl, and F. C. Zach, "Calculation of the passive and active component stress of three phase PWM converter systems with high pulse rate," in *EPE Conf. Rec.*, Aachen, Germany, 1989, pp. 1303–1311.
- [22] L. Abraham and R. Blümel, "Optimization of three phase pulse pattern by variable zero sequence component," in *EPE Conf. Rec.*, Firenze, Italy, 1991, pp. 272–277.
- [23] J. Holtz and B. Beyer, "Optimal pulsewidth modulation for ac servos and low-cost industrial drive," *IEEE Trans. Ind. Applicat.*, vol. 30, pp. 1039–1047, July/Aug. 1994.
- [24] J. Holtz, W. Lotzkat, and A. Kambodkone, "On continuous control of PWM inverters in the overmodulation range including the six-step mode," in *IEEE-IECON Conf. Rec.*, San Diego, CA, 1992, pp. 307–322.
- [25] S. Jul-Ki and S. Sul, "A new overmodulation strategy for induction motor drive using space vector PWM," in *Applied Power Elect. Conf.*, Dallas, TX, Mar. 1995, pp. 211–216.
- [26] A. M. Hava, R. J. Kerkman, and T. A. Lipo, "Carrier-based PWM-VSI overmodulation strategies: Analysis, comparison, and design," *IEEE Trans. Power Electron.*, vol. 13, pp. 674–689, July 1998.
- [27] T. M. Rowan, R. J. Kerkman, and T. A. Lipo, "Operation of naturally sampled current regulators in the transition mode," *IEEE Trans. Ind. Applicat.*, vol. 23, pp. 586–596, July/Aug. 1987.
- [28] A. M. Hava, S. Sul, R. J. Kerkman, and T. A. Lipo, "Dynamic overmodulation characteristics of triangle intersection PWM methods," in *IEEE-Industrial Application Soc. Conf. Rec.*, New Orleans, LA, 1997, pp. 1520–1528.



**Ahmet M. Hava** (S'91) was born in Mardin, Turkey, in 1965. He received the B.S. degree from Istanbul Technical University, Istanbul, Turkey, and the M.S. and Ph.D. degrees from the University of Wisconsin, Madison, all in electrical engineering, in 1987, 1991, and 1998, respectively.

In 1995, he was with Rockwell Automation/Allen Bradley Company, Mequon, WI. He is currently with Yaskawa Electric America, Inc., Waukegan, IL. His research interests include power electronics, electric machines, and control.



**Russel J. Kerkman** (S'67–M'76–SM'88–F'98) received the B.S.E.E., M.S.E.E., and Ph.D. degrees in electrical engineering from Purdue University, West Lafayette, IN, in 1971, 1973, and 1976, respectively.

From 1976 to 1980, he was an Electrical Engineer in the Power Electronics Laboratory of Corporate Research and Development, General Electric Company, Schenectady, NY. He is currently an Engineering Consultant at Rockwell Automation/Allen Bradley, Mequon, WI. His career spans 20 years of industrial experience in power electronics. His current interests include: modeling and control of general-purpose industrial drives, adaptive control applied to field-oriented induction machines, application of observers to ac machines, design of ac motors for adjustable-speed applications, and EMI from PWM inverters. He is a coholder of 15 patents, all in adjustable-speed drives.

Dr. Kerkman is the recipient of seven IEEE Prize Paper Awards. He is a Member of the Industry Applications Society, Industrial Electronics Society, and Power Electronics Society.



**Thomas A. Lipo** (M'64–SM'71–F'87) was born in Milwaukee, WI. He received the B.E.E. and M.S.E.E. degrees from Marquette University, Milwaukee, in 1962 and 1964 and the Ph.D. degree in electrical engineering from the University of Wisconsin, Madison, in 1968.

From 1969 to 1979, he was an Electrical Engineer in the Power Electronics Laboratory of Corporate Research and Development, General Electric Company, Schenectady, NY. He became Professor of Electrical Engineering at Purdue University, West Lafayette, IN, in 1979. In 1981, he joined the University of Wisconsin, where he is presently the W. W. Grainger Professor for Power Electronics and Electrical Machines.

Dr. Lipo received the Outstanding Achievement Award from the IEEE Industry Applications Society in 1986 for his contributions to the field of ac drives, and in 1990, he received the William E. Newell Award of the IEEE Power Electronics Society for contributions to field of power electronics. He received the 1995 Nicola Tesla IEEE Field Award "for pioneering contributions to simulation of and application to electric machinery in solid-state ac motor drives." He has served in various capacities for three IEEE Societies, including being the President of IAS in 1994.